Electrochimica Acta 470 (2023) 143349

Contents lists available at ScienceDirect

Electrochimica Acta

journal homepage: www.journals.elsevier.com/electrochimica-acta

Flow-based compact microfluidic electrochemical cell with Parafilm® channels

Zhenglong Li [a], Niranjan Haridas [a], Maryom Rahman [a], Sreerag Kaaliveetil [a], Yu-Hsuan Cheng [a], Charmi Chande [a], Sagnik Basuray [a,b,*]

[a] Department of Chemical and Materials Engineering, New Jersey Institute of Technology, Newark, NJ 07102, United States
[b] Department of Biomedical Engineering, New Jersey Institute of Technology, Newark, New Jersey 07102, United States

ARTICLE INFO

Keywords:
Parafilm® sheet
Planar interdigitated microelectrode
Microfluidic electrochemical cell
Finite element analysis
Heavy metals

ABSTRACT

A planar interdigitated microelectrodes-based microfluidic electrochemical cell (P-μFEC) with channels made by Parafilm® sheets was conceptualized with the application as a sensor for detecting heavy metal ions. Herein, we first-timely proposed a new strategy for creating **P**arafilm® microchannels using a **P**lotter cutter and **H**ot bonding self-sealing method for solid **M**icrofluidic devices (PPHM). For the prepared novel P-μFEC by the PPHM protocol, which operated in the laminar regime, its electrochemical performance was well-studied using the well-known electrochemical reporter potassium Ferri/Ferrocyanide ($K_3/K_4[Fe(CN)_6]$). A reference electrode (RE) layer deposited at the top silica glass substrate was embedded within the device to minimize the ohmic drop (iR_{cell}) between the working electrode (WE) and RE. The experimental and virtualized computational COMSOL results demonstrated: (**i**) The changes in the RE's placements had negligible influences on the P-μFEC's electrochemical performance. (**ii**) The laminar flow's influence on the P-μFEC's electrochemical performance was quite prominent, which was due to the changes in the mass transfer process from diffusion (stationary) to diffusion + convection (hydrodynamic). (**iii**) A direct virtualized demonstration of laminar flow's influences on the mass transfer process from diffusion (stationary) to diffusion + convection (hydrodynamic) was first timely validated by finite element analysis simulation using COMSOL Multiphysics. (**iv**) Finally, the proposed P-μFEC showed promise as a sensitive electrochemical sensor for different heavy metal ion substrate (model analytes) detection. The IUPAC detection limits for Cu^{2+}, Pb^{2+}, $[Fe(CN)_6]^{3-}$ and Hg^{2+} is ~318.6±3.55 μg/L, ~191±5.4 4 μg/L, ~113.5±9.9 μg/L, and 8.21±0.88 μg/L, respectively. Among them, the detection limit for Cu^{2+} and Hg^{2+} meets the US Environmental Protection Agency (EPA)'s water contamination level for Cu (1300 μg/L) and is close to the EPA level for Hg (2 μg/L), respectively. These findings demonstrate the potential of using the Parafilm® sheet as the microfluidic channel for a flow-based P-μFEC as a novel analytical tool.

1. Introduction

Microfluidic devices have attracted intensive interest in numerous applications as they offer rapid manipulation of solutions, minimum consumption of reagents, low cost, and the ability to perform a wide range of chemical and biological reactions with a small and portable form factor [1]. Furthermore, electrochemical detection techniques are well suited to miniaturized systems due to their compatibility with microfabrication technologies, rapid analysis, cost-effectiveness, and simplicity [2]. Therefore, microfluidic electrochemical cells (hereafter μFECs) as miniaturized analytical devices are receiving increasing attention at the forefront of the development of modern micro total analysis systems and lab-on-a-chip platforms [3–5]. Microelectrodes (μE) fabricated by lithographic technique on silicon or glass substrates have been of great interest in μFECs since they could offer higher sensitivity than macroelectrodes of conventional size due to the smaller area-edge effects [6]. Therefore, the μE-based μFEC are receiving increasing attention in various analytical fields, ranging from inorganic [3,4], organics [7], electrodeposition [8], and even radiological analytes [5].

Polymers, such as polydimethylsiloxane (PDMS) and double-sided polyester tapes, have been widely used to fabricate microfluidic channels [9,10]. While the often-cited advantages of PDMS include low surface interfacial free energy, gas permeability, and large elasticity, the

* Corresponding author.
E-mail address: sbasuray@njit.edu (S. Basuray).

https://doi.org/10.1016/j.electacta.2023.143349
Received 14 June 2023; Received in revised form 5 October 2023; Accepted 11 October 2023
Available online 14 October 2023

fabrication of PDMS replicas is a multistep, time-consuming method that is not ideal for fast prototyping μFECs [11]. The fabrication of microfluidic channels using double-sided tapes is more favorable as they allow for dimensionally stable and mechanically robust components while greatly simplifying the manufacturing process and saving time during replication [12]. However, for the commercially available double-sided tapes, the cost is still expensive for researchers in a resource-limited situation. For example, for the double-sided tape (ARcare® 90106NB), one roll of 9″ x 30′ (width x length) will cost around $300.

Parafilm® sheet is one kind of thermoplastic whose chemical and mechanical properties have been well characterized [13]. Parafilm® sheets mainly contain polyolefins and waxes, melting at around 60 °C. A cheap and rapid method has recently been developed for fabricating paper-based microfluidic analytical devices (μPADs) using Parafilm® thermoplastic sheets [14,15]. For example, Koesdjojo et al. successfully demonstrated a colorimetric microfluidic device using Parafilm® infused paper for detecting heavy metal ion substrates [16]. In a more recent work reported by Kim et al., the preparation of a 3D push-on valve was demonstrated using Parafilm® infused paper [17]. The basic principle of using Parafilm® sheet in μPADs is that with a relatively high applied temperature and pressure (usually a few MPa), the melted Parafilm® wax will penetrate the cellulose fiber networks of paper. As the temperature decreases, the melted wax will become solid again, forming hydrophobic barriers within the paper networks. However, using Parafilm® sheet in μPADs to prepare hydrophobic barriers also faces some drawbacks. One of the limitations is the deformation of the hydrophobic barriers caused by the lamination/pressing process and the inhomogeneity of the porous paper structure [15,17,18]. Furthermore, due to the high-pressure requirement, the thermal lamination/pressing approach is unsuitable for preparing solid substrates (Like silica glass, silicon, polymethyl methacrylate (PMMA)) based microfluidic devices. Because so far, silica glass and silicon are two of the most used substrates to perform various μE layers or dielectric depositions [19,20]. Therefore, a strategy for properly using Parafilm® sheet in solid substrate-based μFECs is needed.

Inspired by these interesting previous works and based on the principle of "do-it-yourself," cost-effective, and rapid prototyping. In this paper, we present for the first time a new rapid strategy for creating **P**arafilm® microchannels using a **P**lotter cutter and **H**ot bonding self-sealing method for solid **M**icrofluidic devices (PPHM). A fully integrated planar interdigitated μEs (P-IDμEs)-based μFEC (hereafter P-μFEC) is prepared by the new PPHM strategy. The electrochemical performance of the proposed P-μFEC was well-studied using the well-known electrochemical reporter potassium Ferri/Ferrocyanide ($K_3/K_4[Fe(CN)_6]$). It is well documented that the placements of the reference electrode (RE) with respect to the working electrode (WE) significantly affect μFECs' sensitivity because of the ohmic drop (iR_{cell}) [21–24]. In addition, mass transfer plays a significant role in the electrochemical process, bringing the electroactive analytes to the WE surface in three different ways (diffusion, migration, and convection). For the μFECs which operate in the laminar regime, the effect of laminar flow on the P-μFEC's electrochemical performance is worth investigating. Therefore, in this work, the influence of RE's placement on the electrochemical performance of Parafilm®-based P-μFEC via the proposed PPHM protocol has been thoroughly studied under stationary and hydrodynamic working conditions. Finally, as a proof-of-concept design, the fully integrated P-μFEC was employed for detecting heavy metal ions. Lead (Pb) and Mercury (Hg) as two representatives of highly toxic metals, Copper (Cu) is one representative of essential metals, and one Hexacyanoferrate(III) ($[Fe(CN)_6]^{3-}$) is analyzed as the model analytes.

2. Experimental Section

2.1. Chemicals and Equipment

Potassium nitrate (KNO_3), 99%, was purchased from Thermo Fisher Scientific. Potassium chloride (KCl) was ordered from Sigma-Aldrich. Potassium Ferri/ferrocyanide ($K_3/K_4[Fe(CN)_6]$) (99.0% min Crystalline) was obtained from Sigma-Aldrich. Copper(II) chloride dihydrate (99%), Lead(II) nitrate (99.0% min), and Mercury (II) chloride (98+%) were purchased from Thermo Fisher Scientific. The de-ionized (DI) water used in the experiments was obtained from a Milli-Q® Direct 8 Water Purification System. Parafilm® wrapping sheet was ordered from Thermo Fisher Scientific. Commercially available water-soluble food dyes from Modern Biology Inc are purchased for the microchannel characterizations. Super glue from Loctite® was used to glue the tube connector to the glass substrates. Acetone (≥ 99.5%, ACS) and isopropyl alcohol (99%, ASC) were purchased from VWR Chemicals BDH® and used to clean chips and separate glass substrates for future assembly. The μEs and microchannel characterization of assembled devices was conducted using Scanning Electron Microscope (SEM, Model: JSM-7900F SEM) and an optical microscope (Olympus BX51). The element distribution was characterized by Energy Dispersive X-ray (EDX) microanalysis (Model: JSM-7900F SEM). The glass slides 75 mm x 25 mm x 1 mm (height x width x length) were used as the deposition substrates purchased from Globe Scientific Incorporated. The electrochemistry characterizations were obtained using a Gamry (Reference 600+) potentiostat. The NE-300 syringe pump from New Era Pump Systems, Inc. (USA) was used to pass the solutions through the microchannels.

2.2. Preparation of Fully Integrated P-μFEC Transducer by PPHM Strategy

μEs were prepared at the Nanofabrication Facility Advances Science Research Center at the City University of New York. Standard lithography techniques were used for patterning [10,25]. Here, glass slides were chosen as the μE deposition substrates. A Chromium (Cr, 10 nm)/Platinum (Pt, 100 nm) multilayer was deposited by Electron Beam Evaporator. Each μE array contains ~250 electrode digits, and each electrode digit has dimensions of 500 μm x 10 μm x 110 nm in length x width x height, respectively. Here, the WE and counter electrode (CE) array are "interdigitated." The gap between adjacent WE and CE digit is around 10 μm, as shown in Fig. 1.

Here we used the Parafilm® sheet as the microchannel layer, as shown in Fig. 2. The proposed PPHM strategy was employed to prepare the device. The general process is as follows: (**1**) Briefly, a Cricut® machine (No: CXPL0001) was first used to obtain the pre-designed channel, which has a 40.6 mm length and 500 μm width (Parafilm® Sheet's thickness is ~130 μm). (**2**) Then, the film was transferred from the cutting mat to the bottom WE and CE layer under the optical microscope. After that, the top RE layer was applied to cover the fluid channel. (**3**) the assembled device was subsequently placed onto a hot plate (~70 °C) for around 2 min for self-sealing. After sealing, the super glue bonded the tube connector to the pre-drilled holes in the top RE layer. Finally, New Era pumps passed the target analyte solutions through the microchannel. The optical and corresponding cross-section SEM images of the Parafilm® microchannel are shown in Figs. 2(b)–(d). The findings observed in Figs. 2(b) and (c) show us highly uniform dimensions along the microfluidic channel and proper adhesion in hybrid systems composed of different layers. Fig. 2(d) explicitly shows the microchannel with a dimension of 500 μm x 130 μm in width x height. The fluorescence images of the Parafilm® microchannel are demonstrated in Figure S1. The picture shows excellent sealing performance with no leakage problems. The total fabrication time was less than 10 minutes, which is attractively easy to design and fabricate versatile structures with this simple thermal fusion protocol.

2.3. Configurations of the Electrodes

For the three-electrode configuration, when the RE is faced against the WE and CE (WE_1/CE_1/RE_1), the horizontal distance is 0 μm while the vertical distance is around 130 μm (i.e., the height of the fluid

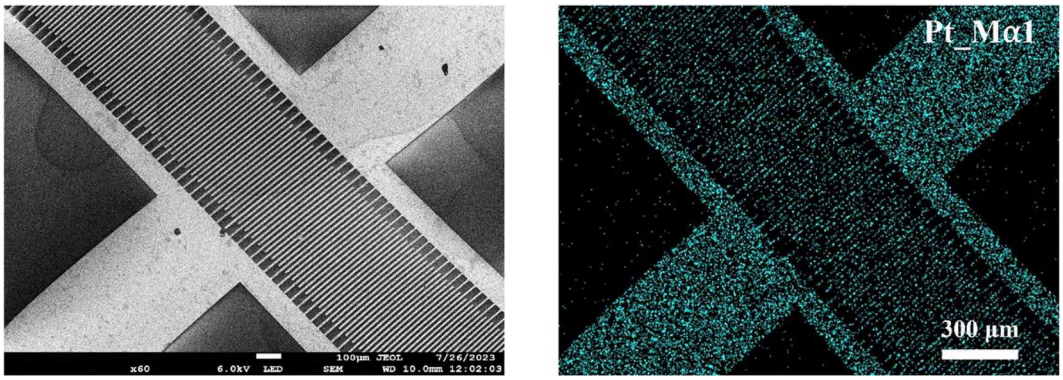

Fig. 1. (**Left**) SEM image of Pt P-IDμE. (**Right**) Corresponding element distribution image of Pt.

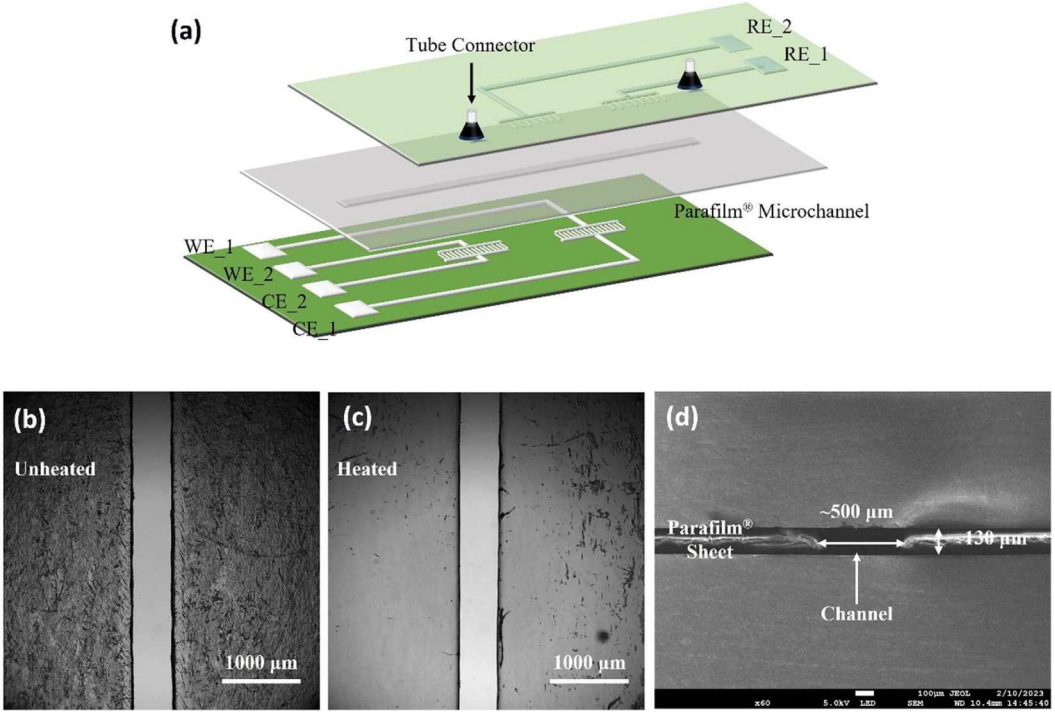

Fig. 2. (a) Schematic diagram of the prepared P-μFEC device. Optical image of Parafilm® microchannel in assembled device (b) unheated and (c) heated. (d) Cross-section SEM image of Parafilm® microchannel in heated assembled P-μFEC device.

channel layer). When the RE is placed away from the WE and CE (Like WE_1/CE_1/RE_2), the horizontal distance is 10 mm, and the vertical distance is still 130 μm.

3. Results and Discussion

3.1. Preparing P-μFEC via PPHM Protocol

Fig. 1(a) shows the structure of prepared P-μFEC using the PPHM protocol. Unlike the use of Parafilm® sheet in μPADs, the proposed PPHM protocol is more applicable to preparing solid substrate-based microfluidic devices. (**i**) Since there is no need to apply high pressure during the preparation process, it avoids the microchannels' deformation and makes it applicable to brittle solid substrates. (**ii**) The heat-assisted self-sealing or packaging process takes around 2 min, significantly reducing the entire preparation time to about 10 min. (**iii**) Since, during the preparation process, there is no need to use a hot-pressing machine and a relatively expensive laser cutter, the proposed PPHM protocol can significantly reduce the preparation cost. It is found for our P-μFEC device, with a 70 °C sealing temperature, the top glass slide's gravity was enough to squeeze out the tiny air bubbles between the Parafilm® film and the glass slides, finishing the self-packaging process. As shown in Figs. 2(b) and (c), compared to the unheated device, the contacted areas between the Parafilm® sheet layer and glass slides were more transparent in the heated device. This is due to removing the tiny air bubbles from the hybrid sandwiched structure of "glass-Parafilm®-glass." Meanwhile, negligible geometry deformation in the Parafilm® film's microchannel layer was found.

3.2. Electrochemical Characterization of P-μFEC

3.2.1. Influences of the RE's Placements on the P-μFEC's Electrochemical Performance

From Figs. 3(a) and 3(b), under the stationary condition, it was found that for the pure electrolyte (0.1M KNO_3), there are no or negligible changes in either CV or DPV background. However, the changes become relatively obvious with the flow (~100 μL/min), especially in the background CV results. Figs. 3(c) and 3(d) are the redox probe results

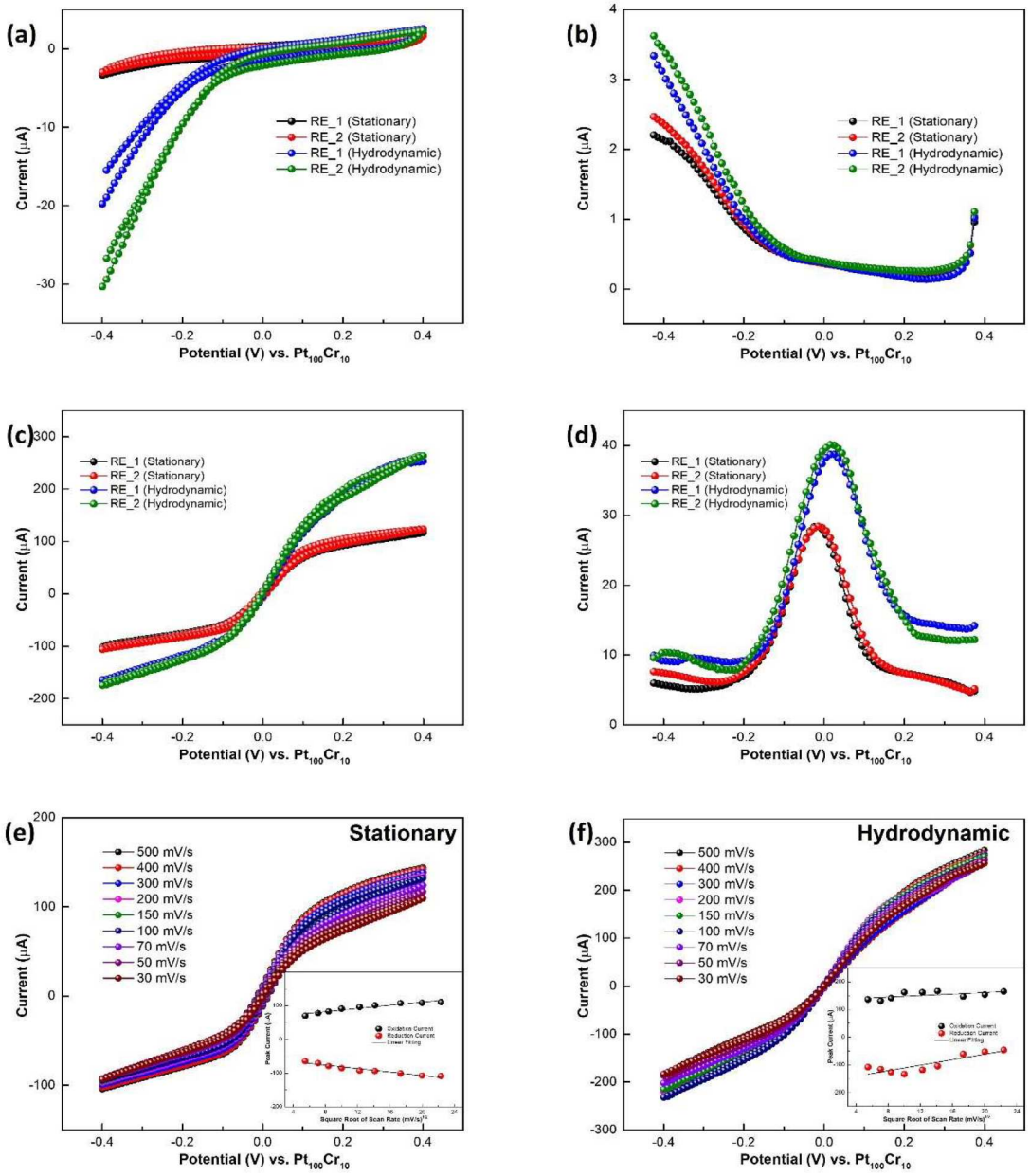

Fig. 3. Here, RE_1 and RE_2 represent the WE_1/CE_1/RE_1,2, respectively. For CV testing, a $\boldsymbol{\nu}$ of 100 mV/s was applied. (a) CV and (b) DPV results were obtained under stationary and hydrodynamic (flow rate = 100 μL/min) conditions using 0.1 M KNO_3 electrolyte. Similarly, for (c) and (d), the solution was changed to 10 mM $K_3/K_4[Fe(CN)_6]$. (e) CV results obtained under stationary condition with different $\boldsymbol{\nu}$. Inset: Peak current plots (I_{pa}, I_{pc}) vs. $\boldsymbol{\nu}^{1/2}$. The equation of the anodic peak current (I_{pa}) line is: I_{pa} (μA) = 2.35 x $\boldsymbol{\nu}^{1/2}$ + 63.6; Coefficient of determination (R^2) = 0.91. The equation of the cathodic peak current (I_{pc}) line is: I_{pc} (μA) = −2.58 x $\boldsymbol{\nu}^{1/2}$ – 55.74; R^2 = 0.94. (f) CV results obtained under hydrodynamic condition with different $\boldsymbol{\nu}$. Inset: (I_{pa}, I_{pc}) vs. $\boldsymbol{\nu}^{1/2}$. Here, for (e) and (f) the results were based on the WE_1/CE_1/RE_1 configuration.

under different flow conditions. As shown in Fig. 3(c), for the two electrode configurations (WE_1/ CE_1/RE_1 and WE_1/CE_1/RE_2, under stationary working conditions), the voltammograms of 10 mM $K_3[Fe(CN)_6]$ and $K_4[Fe(CN)_6]$ (1:1, mole ratio) in KNO_3 (100 mM) at a scan rate ($\boldsymbol{\nu}$) of 100 mV/s show oxidation at anodic peak potential (E_{pa}) of ~140 mV and a back reduction at cathodic peak potential (E_{pc}) at ~-70 mV vs. $Pt_{100}Cr_{10}$ RE. Such that the peak-to-peak separation (ΔE_p) is *ca.* 210 mV. Here, the $\boldsymbol{I}$ (current) vs. $\boldsymbol{E}$ (applied potential) profile at $\boldsymbol{\nu}$ = 100 mV/s shows a sigmoidal behavior reminiscent of a redox cycling electrochemical process characteristic [26]. In this case, $[Fe(CN)_6]^{3-/4-}$ gets reduced/oxidized between the WE and CE electrode digits. The redox cycling counteracts the further depletion of $[Fe(CN)_6]^{3-}$ (cathodic sweep) and $[Fe(CN)_6]^{4-}$ (anodic sweep) near the WE surface and results in steady-state rather than a gradual decrease in the current. With flow (~100 μL/min), the voltammogram changes between two electrode configurations are still negligible. However, compared to the stationary voltammograms, a higher ΔE_p of ~300 mV (E_{pa} = 130 mV and E_{pc} = -170 mV) and higher steady-state current plateaus are observed in the hydrodynamic case. It is confirmed that with the introduction of flow or forced convection, more $[Fe(CN)_6]^{3-/4-}$ analytes are brought to the WE surface, which can further result in a higher current density [6]. As for the increase in the ΔE_p, this usually indicates that the introduction of convection results in a high barrier to electron transfer between the WE and CE electrode digits, and electron transfer reactions are sluggish [27]. Hence more negative (positive) potentials are required to observe reduction (oxidation) reactions, giving rise to more significant ΔE_p.

For the differential pulse voltammograms shown in Fig. 3(d), it is found that under either stationary or hydrodynamic conditions, the changes in the RE's placement have a negligible effect on the reduction peak. Under the stationary condition, a typical voltammogram of the $[Fe(CN)_6]^{3-/4-}$ couple appears at a peak potential (E_{peak}) of *ca.* -18 mV with a full width at half maximum (FWHM) of ~160 mV. Similarly, based on the WE/CE_1/RE_2, an FWHM of ~160 mV is observed. Under the hydrodynamic condition, a typical voltammogram at E_{peak} of *ca.* 17 mV with an FWHM of ~190 mV is observed. Similarly, based on the WE_1/CE_1/RE_2, an FWHM of ~205 mV is also observed. Compared with the stationary case, a right shift in the reduction peak is observed (from –18 to 17 mV).

The above findings demonstrate that (**i**) the changes in the RE's placements will not influence the final device's electrochemical performance. This demonstrates that our proposed device structure, P-μFEC, has relatively high flexibility on the placement of the RE. (**ii**) Howeperver, the influence of laminar flow on the final device's electrochemical performance is significant. Here, since the ionic strength of 10 mM $K_3/K_4[Fe(CN)_6]$ redox probe + 100 mM, KNO_3 is around 0.42 M, which is much higher than 0.2 M [26]. Therefore, the influence of electromigration has been excluded from this study. Hence, it is hypothesized that the changes to the electrochemical performance of P-μFEC are due to the mass transfer process from diffusion (stationary) to diffusion + convection (hydrodynamic).

3.2.2. *Influences of Laminar Flow on the P-μFEC's Electrochemical Process*

To further confirm the above hypothesis, the effect of ν on peak currents of the cyclic voltammograms was monitored. From Fig. 3(e), it is observed that for all the ν studied, from 30 to 500 mV/s, the cathodic and anodic processes' peak currents (I_{pc}, I_{pa}) vs. the square root of scan rate ($\nu^{1/2}$) show good adherence to linearity, demonstrating classical Nernstian diffusion-controlled redox behavior [10,28].

$$i_p = 0.446nFAC^o\left(\frac{nF\nu D_0}{RT}\right)^{1/2} \quad (1)$$

The Randle-Sevcik Equation (1) can calculate the cumulative active electrode surface area (A_{active}). Using the literature value of diffusion coefficients (7.3×10^{-6} cm^2/s for $[Fe(CN)_6]^{3-}$ [28]; 6.3×10^{-6} cm^2/s for $[Fe(CN)_6]^{4-}$ [29]), the corresponding A_{active} are determined as 1.21×10^{-2} cm^2 and 1.39×10^{-2} cm^2, respectively. These calculated values agree with the actual cumulative geometrical surface area (A_{geom}, $\sim 1.25 \times 10^{-2}$ cm^2) of the $Pt_{100}Cr_{10}$ WE. However, from Fig. 3(f), instead of seeing a linear relationship between peak currents (I_{pc}, I_{pa}) and $\nu^{1/2}$, a non-linear relationship is observed, demonstrating that the electrochemical process under the hydrodynamic condition is not a diffusion-controlled redox behavior. Therefore, the non-linear relationship observed in Fig. 3(f) is due to the combined mass transfer process, the diffusion + convection-controlled redox behavior.

The laminar flow's influence on the P-μFEC's electrochemical performance under the AC working mode was characterized, and relevant electrochemical impedance spectroscopy (EIS) is shown in Fig. 4. The Nyquist and Bode plots of P-μFEC under stationary and hydrodynamic working conditions are shown in Figs. 4(a) and (b), respectively. Based on the Nyquist and Bode plots, one equivalent circuit was proposed to model the EIS signatures. In this equivalent circuit (Fig. 4(c)), a R_c resistor represents the solution resistance filling between the WE and CE electrode fingers. $\mathbf{C_{dl}}$ is the double-layer capacitance in the interface between the redox solution and μEs. $\mathbf{R_{ct}}$ is the charge transfer resistance associated with the electrons' transfer from the redox solution onto the μEs. $\mathbf{R_{ct}}$ and diffusion process related Warburg impedance (**W**) are modeled parallel to $\mathbf{C_{dl}}$ as co-occurring phenomena [30,31]. Based on the proposed equivalent circuit, the relevant simulated results are shown in Table 1. With the turn-on of flow, a decrease in the $\mathbf{R_{ct}}$ is observed. Therefore, it is concluded that the turn-on of flow facilitates rapid charge transfer between adjacent μE fingers of P-μFEC.

3.3. *Finite Element Analysis of Laminar Flow's Influence on P-μFEC's Electrochemical Process*

Laminar flow plays an important role in the P-μFEC's electrochemical performance. Therefore, a visualized demonstration of laminar flow's influence on the concentration distribution of 10 mM $K_3/K_4[Fe(CN)_6]$ was conducted through finite element analysis (FEA) using COMSOL Multiphysics 5.5. To avoid long pre-processing, solving, and post-processing periods, the cross-section image of the P-μFEC along the channel is simplified to a representative 2D model, as shown in Figs. 5(a) and 5(b) [10,32]. The periodic distribution characteristics of P-IDμE further reduce the model to a few representative pairs of electrode digits (Fig. 5(b)). The width and gap of the electrode digits are set to 10 μm. A view of the mesh discretization network with a high resolution is shown

Table 1
Value of Each Element in the Equivalent Circuit.

Condition	R_c (ohm)	C_{dl} (F)	R_{ct} (ohm)	Warburg (S-sec$^{0.5}$)	Chi-square
Stationary	69.8	2.773E-8	425.7	4.57E-5	2.57E-3
Hydrodynamic	69.6	2.413E-8	404.4	5.03E-5	2.53E-3

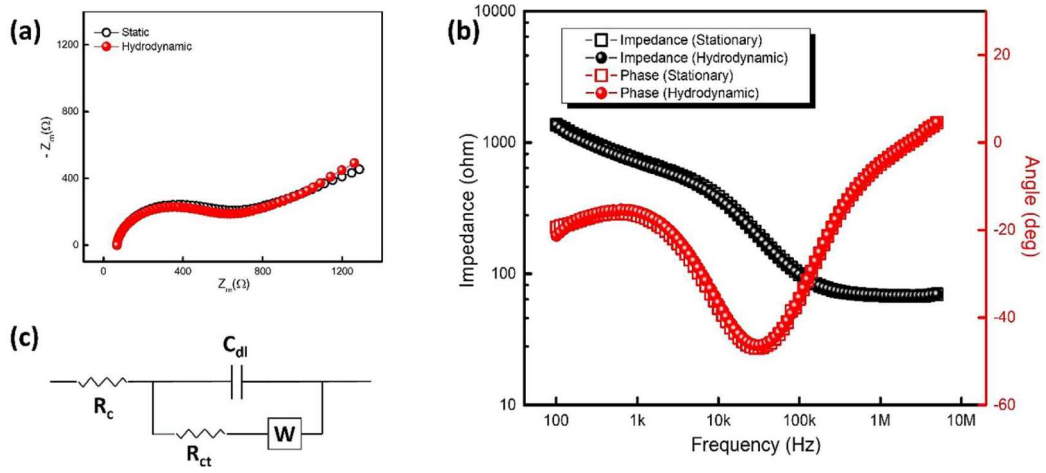

Fig. 4. (a) Nyquist plots and corresponding (b) Bode plots of P-μFEC obtained at WE_1/CE_1/RE_1 electrode configuration. (c) Equivalent circuit diagram. The solution is 10 mM $K_3/K_4[Fe(CN)_6]$ redox probe in 100 mM KNO_3.

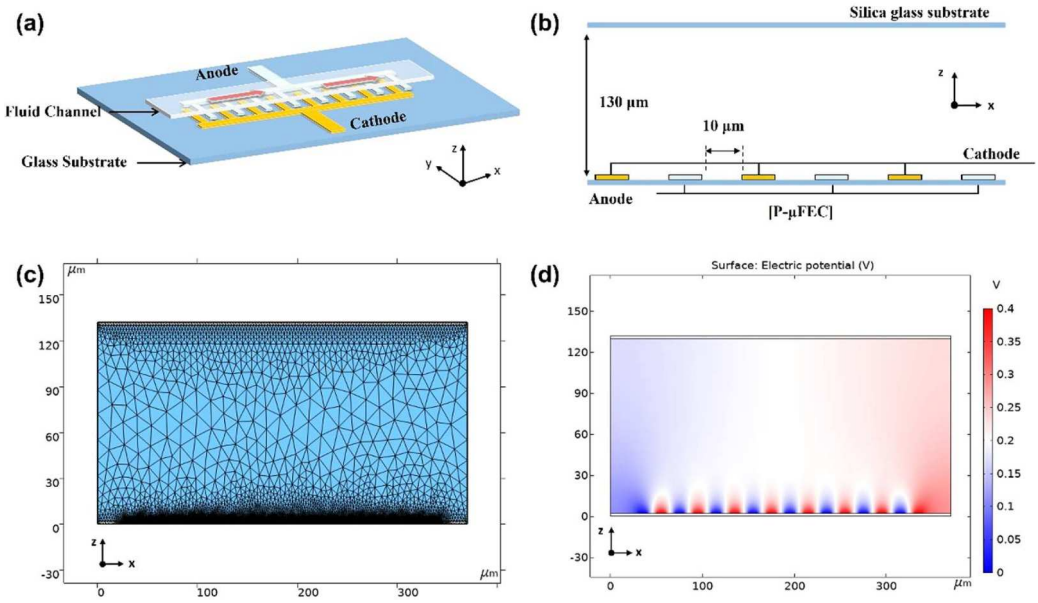

Fig. 5. (a) Schematic diagram of P-μFEC. (b) Geometry information of P-μFEC. (c) Time-dependent electrical potential profile of the WE surface. (c) One representative mesh discretization network of the P-IDμE. (d) Image of electric potential profile around the electrodes obtained through simulation with COMSOL platform.

in Fig. 5(c). The time-dependent electrical potential profile was added onto the WE surface (Figure S2). The simulation of the electrical potential in the vicinity of the WE is shown in Fig. 5(d).

Time-dependent COMSOL simulations of $K_3/K_4[Fe(CN)_6]$'s concentration distribution profiles were recorded under different flow rates. It is important to note that for this simulation, Butler-Volmer electrode kinetics are chosen [33]. The $[Fe(CN)_6]^{3-/4-}$ bulk solution concentration keeps at ~10 mM. The forward and backward reactions are characterized by the rate constant k_f and k_b, respectively. The forward and backward reaction rates on the WE are described as follows:

$$N_f = k_f C_O \tag{2}$$

$$N_b = k_b C_R \tag{3}$$

where N_f and N_b are the mass flow density expressed as the number of moles crossing the unit surface in the time unit. The Butler-Volmer electrode reaction kinetics describes the reaction rate constants at the electrodes as follows:

$$k_f = k_s e^{-\alpha(E-E_0)\frac{F}{RT}} \tag{4}$$

$$k_b = k_s e^{1-\alpha(E-E_0)\frac{F}{RT}} \tag{5}$$

where k_s is the standard rate constant and α the transfer coefficient. In symmetrical reactions, α has a value of 0.5. E is the applied voltage on the electrode surface, and E_0 has a value of 0 V. *F*, *R*, and *T* are the Faraday constant (9.64853×10^4 C/mol), molar gas constant (8.3144 J/(mol*K)), and temperature (298 K), respectively.

Figs. 6(a1) and (a2) are simulated results under stationary conditions. From Figs. 6(a1) and (a2), we can directly observe that $[Fe(CN)_6]^{3-/4-}$ got reduced/oxidized between the WE and CE digits. This process is sometimes called "redox cycling" due to the overlap of their diffusion regions [26]. The direct observation of "redox cycling" perfectly explains the appearance of sigmoidal cyclic voltammograms in P-μFEC (Fig. 4(c)). With the turn-on of the flow (hydrodynamic conditions), an apparent attenuation in the diffusion domain was observed due to the introduction of forced convection (Figs. 6(b1) and (b2)). With further increases in the flow rate, the attenuation in the diffusion domain becomes more apparent, as shown in Figs. 6(c1) and (c2) insets. These simulated findings further confirm that the reason that caused the decrease in **Cdl** value is the disruption of the diffusion dynamics of reagents (Table 1). However, it is also found that the laminar flow will not be able to interrupt the "redox cycling" electrochemical process. This explains why even when the flow rate was increased to 100 μl/min, sigmoidal cyclic voltammogram curves were still observed in Fig. 4(c).

3.4. Heavy Metal Ion Substrate Detection

As a proof-of-concept, the fully integrated P-μFEC was used as an electrochemical sensor for detecting aqueous heavy metal samples, as the primary source of human exposure to heavy metals is from contaminated water. In this work, Lead (Pb) and Mercury (Hg) as two representatives of highly toxic metals, Copper (Cu) is one representative of essential metals, and one Hexacyanoferrate(III) ($[Fe(CN)_6]^{3-}$), were analyzed as the model analytes. Under the hydrodynamic working conditions (100 μL/min), the differential pulse voltammograms for different metallic ions were collected and shown in Figs. 7 and S3.

Fig. 7(a) shows the typical voltammograms for the aqueous Pb^{2+} solutions, with an E_{peak} located at *ca.* -0.7 V. A gradual increase in the DPV reduction peak currents with the gradual rise in the Pb^{2+} concentration is observed. The standard errors were calculated based on the results shown in Fig. 7(a) and repeated DPV testing shown in Figure S4 (a). Here, the standard error is assumed due to the difference in the surface area of the μEs from chip to chip during the device fabrication process, as has been reported elsewhere [34,35]. The errors are within the tolerance expected from lab-based experiments that show a proof-of-concept. As a result, the calibration curve's linear portion falls from 5 to 0.1 mg/L with a high coefficient of determination (R^2) equal to 0.994, as shown in Fig. 7(b). Therefore, a preliminary value of the ***DL*** can be calculated based on the IUPAC recommended formula (Eq. 6) [36].

$$\boldsymbol{DL} = \frac{K * S_b}{m} \tag{6}$$

Here, ***K*** is a numerical constant, ***m*** is the slope of the plot's linear region, and $\mathbf{S_b}$ is the standard deviation of the blank or the ordinate intercept standard deviation [37]. According to IUPAC recommendations, a ***K*** value of 3 corresponds to a 99.87% confidence level was used

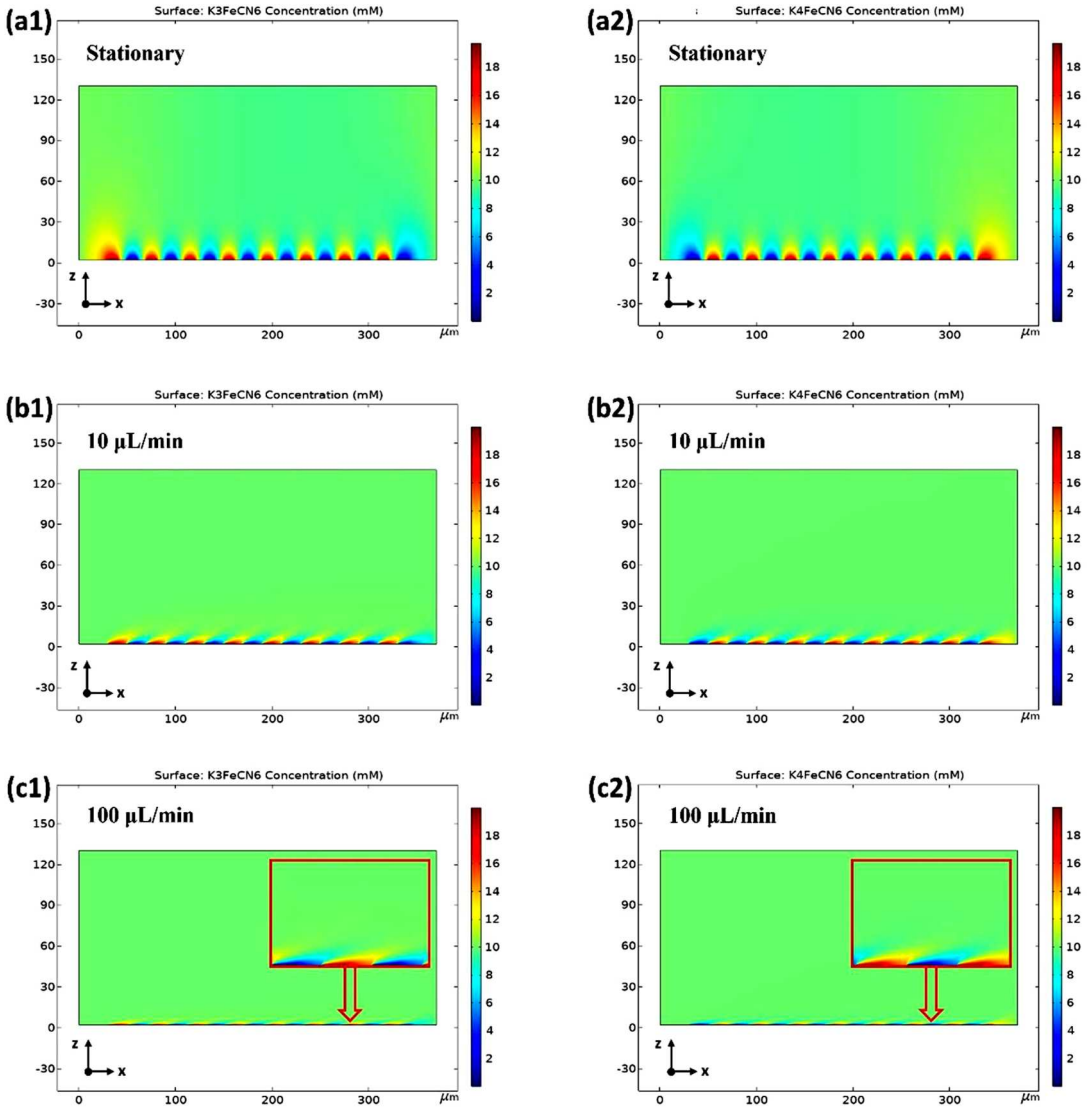

Fig. 6. The simulated concentration distribution profiles of $K_{3/4}[Fe(CN)_6]$ within the channel of P-µFEC under different flow rates (a1) and (a2) at a flow rate of 0 µL/min (Stationary); (b1) and (b2) at a flow rate of 10 µL/min (Hydrodynamic); (c1) and (c2) at a flow rate of 100 µL/min (Hydrodynamic).

[4]. Therefore, a ***DL*** of ~191±5.4 µg/L is obtained for aqueous Pb^{2+} analyte. For Cu^{2+}, two reduction peaks ranging from -0.2 to -0.4 V are observed, which is hypothesized to be related to the reduction process from Cu^{2+} to Cu (Figs. 7(c) and S4(b)). For the aqueous Cu^{2+} solutions, based on the first reduction peak, a linear portion falls from 5 to 0.5 mg/L with an R^2 equal to 0.987, and a ***DL*** of ~318.6±3.5 µg/L is obtained (Fig. 7(d)). Similarly, for the aqueous Hg^{2+} solutions, a ***DL*** of ~8.21±0.8 µg/L is obtained (Figures S3 and S4(d)). However, for the aqueous $[Fe(CN)_6]^{3-}$ solutions, the calibration plot is divided into two segments with different slopes at the inflection point of 1 mg/L. After the concentration of $[Fe(CN)_6]^{3-}$ is greater than 1 mg/L, the growth trend slows down obviously. Based on the conclusions reached by other researchers who have observed such "biphasic response", it can be hypothesized that this "biphasic response" is also due to a dynamic equilibrium between surface adsorption, electrolysis, and deposition [38,39]. Hence, post the inflection point, the sensitivity of the electrode towards $[Fe(CN)_6]^{3-}$ decreases, leading to a change in the slope of the calibration line. The reason for this phenomena might be that $[Fe(CN)_6]^{3-}$ on the electrode surface was in a relatively saturated state [40]. Therefore, the ***DL*** is calculated based on the linear portion falls from 1 to 0.3 mg/L (Figs. 7(e) and S4(c)). Finally, an ***DL*** of ~113.5±9.9 µg/L with an R^2 of 0.988 is obtained as shown in Fig. 7(f).

The differential pulse voltammograms for the mixture of Cu^{2+} and Pb^{2+} aqueous solutions are shown in Fig. 8(a). The reduction peaks of the Cu^{2+} and Pb^{2+} analytes can be easily distinguished, and no interference is observed. However, it should be noted that the reduction peaks from $[Fe(CN)_6]^{3-}$ and Hg^{2+} are partially overlapped with each other (Figs. 7(e) and S3). Therefore, a detailed and comprehensive study of the selectivity of P-µFEC to heavy metal ions with similar redox positions is needed in future work. Relevant statistical results of the IUPAC ***DLs*** for these metal ion substrates are given in Fig. 8(b) and Table 2. Among them, the ***DL*** for Cu^{2+} (~318.6±3.5 µg/L) is below the US EPA's water contamination level for Cu (1300 µg/L), and the ***DL*** for Hg^{2+} (~8.21±0.8 µg/L) approaches the EPA level (2 µg/L). Therefore, it is believed that with further electrode surface modification, as it is beyond the scope of this paper, this demonstrated cost-effective, simple-fabrication Parafilm®-based P-µFEC could be a new analytical tool for other research groups for heavy metal ion fast screening.

4. Conclusions

This work prepared a fully integrated microfluidic electrochemical cell, P-µFEC, using a Parafilm® sheet as the middle microchannel/bonding layer. The successful employment of the Parafilm® sheet as a

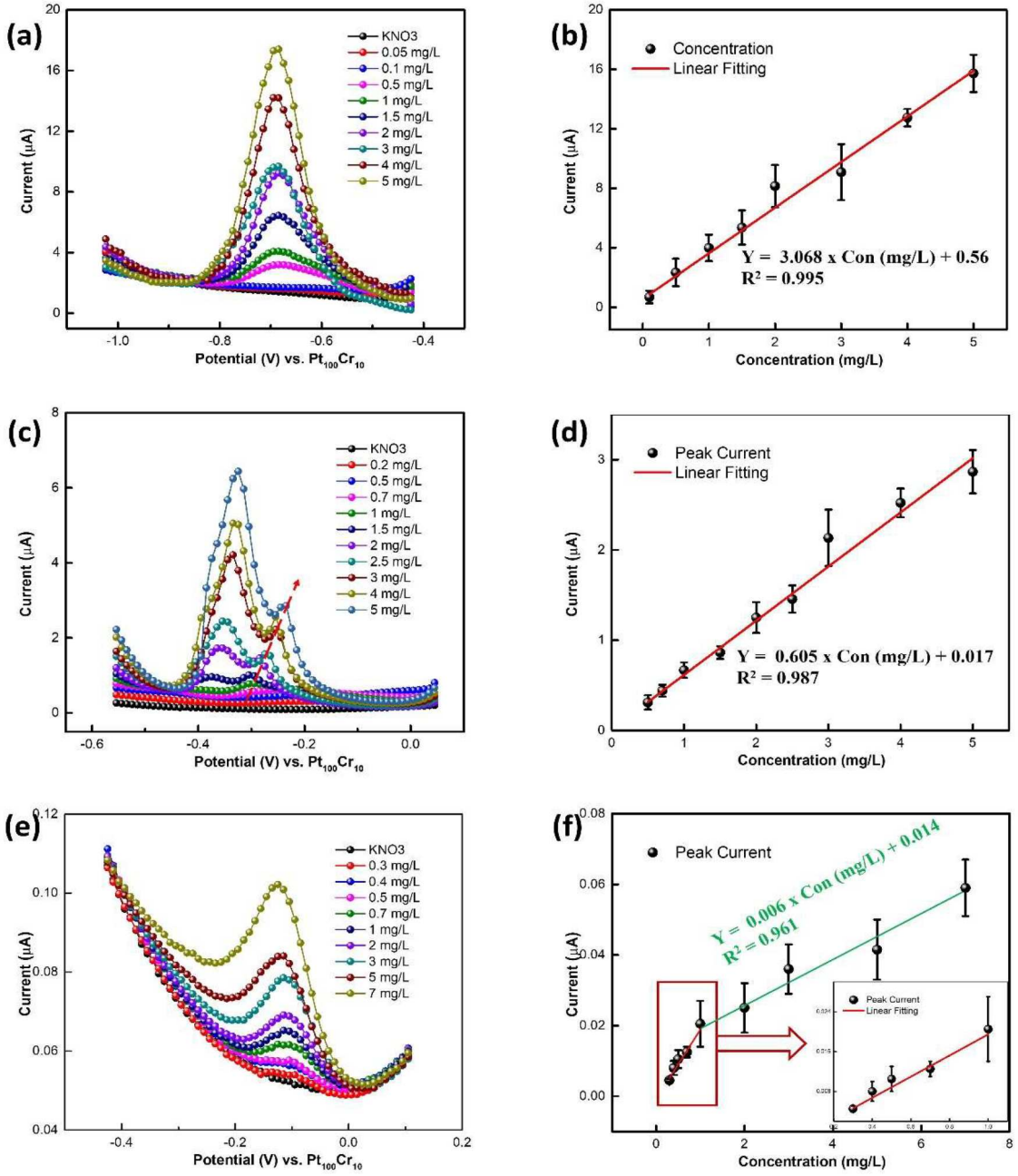

Fig. 7. (a) DPV results for aqueous Pb^{2+}solutions with different concentrations. (b) Corresponding peak current vs. the concentrations of Pb^{2+}. The equation of linear range is $Y = 3.068$ x Con (mg/L) + 0.56; $R^2 = 0.995$. Similarly, for aqueous Cu^{2+}solutions (c), the corresponding linear range equation in (d) is $Y = 0.605$ x Con (mg/L) + 0.017; $R^2 = 0.987$. For aqueous $[Fe(CN)_6]^{3-}$ solutions (e), the corresponding linear range equation (0.3-1 mg/L) is $Y = 0.021$ x Con (mg/L) - 0.002; $R^2 = 0.961$. The corresponding linear range equation (1-5 mg/L) is $Y = 0.006$ x Con (mg/L) + 0.0142; $R^2 = 0.961$. Here, all the results are obtained based on the electrode configuration of WE_1/CE_1/RE_1 or WE_2/CE_2/RE_2 and under the hydrodynamic working conditions (100 μL/min).

middle microchannel and bonding layer had been achieved via the proposed new PPHM protocol. Based on the prepared P-μFEC, the placement of the reference electrode (RE) with respect to the working electrode (WE) was thoroughly studied under stationary and hydrodynamic working conditions. The experimental and computational studies found: (**i**) The changes in the RE's placements had negligible influences on the P-μFEC's electrochemical performance. This is due to the high inertness of the ohmic drop between the WE and RE in the microfluidic devices. (**ii**) The laminar flow's influence on the P-μFEC's electrochemical performance is significant, which is due to the changes in the mass transfer process from diffusion (stationary) to diffusion + convection (hydrodynamic). (**iii**) A direct demonstration of flow's influences on the electrochemical process was validated by finite element analysis simulation using COMSOL Multiphysics.

Finally, the application of our proposed flow-based P-μFEC in detecting heavy metal ions has been carried out. The IUPAC detection limits (***DLs***) for Cu^{2+}, Pb^{2+}, $[Fe(CN)_6]^{3-}$, and Hg^{2+} are ~318.6±3.5 μg/L, ~191±5.4 μg/L, ~113.5±9.9 μg/L and ~8.21±1.1 μg/L, respectively, which meets the US Environmental Protection Agency (EPA)'s water contamination level for Cu (1300 μg/L) and close to the level for Hg (2 μg/L). These findings demonstrate that the proposed cost-effective, simple fabrication, fully integrated P-μFEC via the new PPHM protocol has promising potential as a new electrochemical analytical tool for other research groups for fast heavy metal ions

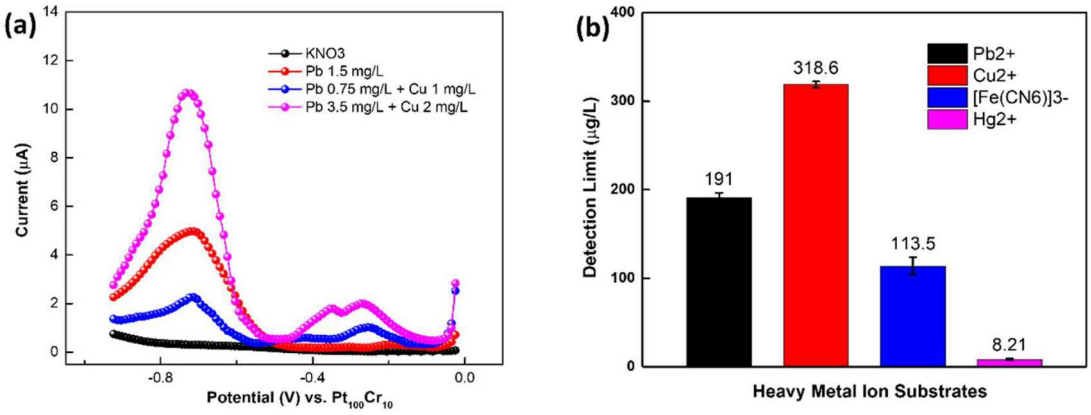

Fig. 8. (a) DPV results from the mixture of different heavy metals with different heavy metal compositions. (b) IUPAC ***DL*** results for Pb^{2+}, Cu^{2+}, and metal compound ($[Fe(CN)_6]^{3-}$) based on the present P-μFEC. Here, all the results are obtained based on the electrode configuration of WE_1/CE_1/RE_1 and under the hydrodynamic working conditions (100 μL/min).

Table 2
Summary of IUPAC Detection Limits for Heavy Metal Ion Substrates.

Analytes	Cu^{2+}	Pb^{2+}	$[Fe(CN)_6]^{3-}$	Hg^{2+}
EPA Level (μg/L)	1300	15	–	2
This Work (μg/L)	318.6±3.5	191±5.4	113.5 ± 9.9	8.21 ± 0.8

screening.

CRediT authorship contribution statement

Zhenglong Li and Maryom Rahman: Experiments, Writing – original and revised drafts, and Conceptualization. **Niranjan Haridas, Sreerag Kaaliveetil, Yu-Hsuan Cheng, and Charmi Chande:** Writing and editing. **Sagnik Basuray:** Writing – review and editing, and Conceptualization.

Declaration of Competing Interest

The authors declare that they have no known competing financial interests or personal relationships that could have appeared to influence the work reported in this paper.

Data availability

Data will be made available on request.

Acknowledgments

This manuscript is supported by Sagnik Basuray's NSF grant # 1751759, Career: "ASSURED" electrochemical platform for multiplexed detection of Cancer Biomarker Panel using Shear Enhanced Nanoporous Capacitive Electrodes; NSF I-Corps grant #2048361, I-Corps: Point-of-use microfluidics-based electrochemical platform for per- and poly-fluoroalkyl substance (PFAS) detection in the source water; NSF REU grant, #2150369, Undergraduate Research and Innovation Experience in Cancer Diagnosis and Therapeutic Intervention; an NJIT 2022 Technology Innovation Translation and Acceleration (TITA) Program Seed Grant Award; a DHS SBIR Phase I and II grant, DHS221-001, "Low-cost Diagnostic for Animal and Zoonotic Diseases".

Supplementary materials

Supplementary material associated with this article can be found, in the online version, at doi:10.1016/j.electacta.2023.143349.

Reference

[1] R. Bogdanowicz, M. Jönsson-Niedziolka, E. Vereshchagina, A. Dettlaff, S. Boonkaew, M. Pierpaoli, P. Wittendorp, S. Jain, F. Tyholdt, J. Thomas, Microfluidic devices for photo-and pectroelectrochemical applications, Curr. Opin. Electrochem. (2022), 101138.
[2] A. Fernandez-la-Villa, D.F. Pozo-Ayuso, M. Castaño-Álvarez, Microfluidics and electrochemistry: an emerging tandem for next-generation analytical microsystems, Curr. Opin. Electrochem. 15 (2019) 175–185.
[3] D. Martín-Yerga, A. Pérez-Junquera, M.a.B.a. González-García, D. Hernández-Santos, P. Fanjul-Bolado, In situ spectroelectrochemical monitoring of dye bleaching after electrogeneration of chlorine-based species: application to chloride detection, Anal. Chem. 90 (2018) 7442–7449.
[4] S. Chatterjee, M.S. Fujimoto, Y.H. Cheng, R. Kargupta, J.A. Soltis, R.K. Motkuri, S. Basuray, Improving the sensitivity of electrochemical sensors through a complementary luminescent mode: a new spectroelectrochemical approach, Sens. Actuators B 284 (2019) 663–674.
[5] S. Chatterjee, S.A. Bryan, C.J. Seliskar, W.R. Heineman, Three-component spectroelectrochemical sensor module for the detection of pertechnetate (TcO4-), Rev. Anal. Chem. 32 (2013) 209–224.
[6] J. Min, A.J. Baeumner, Characterization and optimization of interdigitated ultramicroelectrode arrays as electrochemical biosensor transducers, Electroanalysis: Int. J. Devot. Fund. Practical Aspect. Electroanal. 16 (2004) 724–729.
[7] Y.-T. Li, L.-L. Qu, D.-W. Li, Q.-X. Song, F. Fathi, Y.-T. Long, Rapid and sensitive in-situ detection of polar antibiotics in water using a disposable Ag–graphene sensor based on electrophoretic preconcentration and surface-enhanced Raman spectroscopy, Biosens. Bioelectron. 43 (2013) 94–100.
[8] B. Gomes, L. Nunes, C. Lobo, A. Carvalho, L. Cabeça, L. Colnago, In situ analysis of copper electrodeposition reaction using unilateral NMR sensor, J. Magn. Reson. 261 (2015) 83–86.
[9] B.M.D.C. Costa, S. Griveau, F. d'Orlye, F. Bedioui, J.A.F. da Silva, A. Varenne, Microchip electrophoresis and electrochemical detection: a review on a growing synergistic implementation, Electrochim. Acta 391 (2021), 138928.
[10] Z. Li, Y.-H. Cheng, C. Chande, S. Chatterjee, S. Basuray, A highly sensitive, easy-and-rapidly-fabricable microfluidic electrochemical cell with an enhanced three-dimensional electric field, Anal. Chim. Acta (2022), 340488.
[11] B. Weigl, G. Domingo, P. LaBarre, J. Gerlach, Towards non-and minimally instrumented, microfluidics-based diagnostic devices, Lab Chip 8 (2008) 1999–2014.
[12] P. Gu, K. Liu, H. Chen, T. Nishida, Z.H. Fan, Chemical-assisted bonding of thermoplastics/elastomer for fabricating microfluidic valves, Anal. Chem. 83 (2011) 446–452.
[13] Y. Lu, Z. Shi, L. Yu, C.M. Li, Fast prototyping of a customized microfluidic device in a non-clean-room setting by cutting and laminating Parafilm®, RSC Adv. 6 (2016) 85468–85472.
[14] L. Yu, Z.Z. Shi, Microfluidic paper-based analytical devices fabricated by low-cost photolithography and embossing of Parafilm®, Lab Chip 15 (2015) 1642–1645.
[15] S. Kasetsirikul, K. Clack, M.J. Shiddiky, N.-T. Nguyen, Rapid, simple and inexpensive fabrication of paper-based analytical devices by Parafilm® hot pressing, Micromachines (Basel) 13 (2021) 48.
[16] M.T. Koesdjojo, S. Pengpumkiat, Y. Wu, A. Boonloed, D. Huynh, T.P. Remcho, V. T. Remcho, Cost effective paper-based colorimetric microfluidic devices and mobile phone camera readers for the classroom, J. Chem. Educ. 92 (2015) 737–741.
[17] Y.S. Kim, Y. Yang, C.S. Henry, Laminated and infused Parafilm®–paper for paper-based analytical devices, Sens. Actuators B 255 (2018) 3654–3661.
[18] S.H.S. Tali, H. Hajimiri, Z. Sadiq, S. Jahanshahi-Anbuhi, Engineered detection zone to enhance color uniformity on paper microfluidics fabricated via Parafilm®-heating-laser-cutting, Sens. Actuators B (2023), 133324.

[19] N. Na, M. Zhao, S. Zhang, C. Yang, X. Zhang, Development of a dielectric barrier discharge ion source for ambient mass spectrometry, J. Am. Soc. Mass Spectrom. 18 (2007) 1859–1862.
[20] X. Zhao, C. Hinchliffe, C. Johnston, P.J. Dobson, P.S. Grant, Spray deposition of polymer nanocomposite films for dielectric applications, Mater. Sci. Eng.: B 151 (2008) 140–145.
[21] F. Zhang, J. Liu, I. Ivanov, M.C. Hatzell, W. Yang, Y. Ahn, B.E. Logan, Reference and counter electrode positions affect electrochemical characterization of bioanodes in different bioelectrochemical systems, Biotechnol. Bioeng. 111 (2014) 1931–1939.
[22] Z. Li, J. Ni, S. Zhang, C. Li, Y. Du, Y. Zhang, H. Cai, J. Li, J. Zhang, Effect of incorporation of highly-ordered a-Ge: h nanoparticles on the performance of perovskite solar cells, Micro Nano Lett. 13 (2018) 1111–1116.
[23] S. Cheng, H. Liu, B.E. Logan, Increased performance of single-chamber microbial fuel cells using an improved cathode structure, Electrochem. Commun. 8 (2006) 489–494.
[24] G. Hsieh, T.O. Mason, E. Garboczi, L. Pederson, Experimental limitations in impedance spectroscopy: part III. Effect of reference electrode geometry/position, Solid State Ionics 96 (1997) 153–172.
[25] Z. Li, Y.-H. Cheng, L. Feng, J. Neil, R.M.P. Antonio, M. Rahman, J. Yang, S. Azizighannad, S. Mitra, S. Basuray, Communication—electrochemical impedance signature of a non-planar, interdigitated, flow-through, porous, carbon-based microelectrode, J. Electrochem. Soc. 166 (2019) B1669.
[26] Y. Li, W. Van Roy, L. Lagae, P.M. Vereecken, Effects of counter electrode induced redox cycling on Fe (III) reduction within microfluidic electrochemical cells, J. Electrochem. Soc. 161 (2014) E128.
[27] N. Elgrishi, K.J. Rountree, B.D. McCarthy, E.S. Rountree, T.T. Eisenhart, J. L. Dempsey, A practical beginner's guide to cyclic voltammetry, J. Chem. Educ. 95 (2018) 197–206.
[28] S. Konopka, B. McDuffie, Diffusion coefficients of ferri-and ferrocyanide ions in aqueous media, using twin-electrode thin-layer electrochemistry, Anal. Chem. 42 (1970) 1741–1746.
[29] H.-C. Chang, C.-C. Wu, S.-J. Ding, I.-S. Lin, I.-W. Sun, Measurement of diffusion and partition coefficients of ferrocyanide in protein-immobilized membranes, Anal. Chim. Acta 532 (2005) 209–214.
[30] S. Ding, C. Mosher, X.Y. Lee, S.R. Das, A.A. Cargill, X. Tang, B. Chen, E. S. McLamore, C. Gomes, J.M. Hostetter, Rapid and label-free detection of interferon gamma via an electrochemical aptasensor comprising a ternary surface monolayer on a gold interdigitated electrode array, ACS Sensors 2 (2017) 210–217.
[31] M.S. Abouzari, F. Berkemeier, G. Schmitz, D. Wilmer, On the physical interpretation of constant phase elements, Solid State Ionics 180 (2009) 922–927.
[32] E. Kostal, S. Kasemann, C. Dincer, S. Partel, Impedimetric Characterization of Interdigitated Electrode Arrays for Biosensor Applications, Multidisciplinary Digital Publishing Institute Proceedings, 2018, p. 899.
[33] H.E.Z. Abidin, A.A. Hamzah, B.Y. Majlis, Electrical characterization of Interdigital Electrode based on cyclic voltammetry performances, in: 2012 10th IEEE International Conference on Semiconductor Electronics (ICSE), IEEE, 2012, pp. 348–351.
[34] J.S. Swensen, Y. Xiao, B.S. Ferguson, A.A. Lubin, R.Y. Lai, A.J. Heeger, K. W. Plaxco, H.T. Soh, Continuous, real-time monitoring of cocaine in undiluted blood serum via a microfluidic, electrochemical aptamer-based sensor, J. Am. Chem. Soc. 131 (2009) 4262–4266.
[35] B.S. Ferguson, S.F. Buchsbaum, J.S. Swensen, K. Hsieh, X. Lou, H.T. Soh, Integrated microfluidic electrochemical DNA sensor, Anal. Chem. 81 (2009) 6503–6508.
[36] G.L. Long, J.D. Winefordner, Limit of detection. A closer look at the IUPAC definition, Anal. Chem. 55 (1983) 712A–724A.
[37] A. Shrivastava, V.B. Gupta, Methods for the determination of limit of detection and limit of quantitation of the analytical methods, Chronicl. Young Sci. 2 (2011) 21.
[38] J. Zhong, H. Zhao, Y. Cheng, T. Feng, M. Lan, S. Zuo, A high-performance electrochemical sensor for the determination of Pb (II) based on conductive dopamine polymer doped polypyrrole hydrogel, J. Electroanal. Chem. 902 (2021), 115815.
[39] M. Hu, H. He, F. Xiao, C. Liu, Bi-MOF-derived carbon wrapped Bi nanoparticles assembly on flexible graphene paper electrode for electrochemical sensing of multiple heavy metal ions, Nanomaterials 13 (2023) 2069.
[40] C. Guo, C. Wang, H. Sun, D. Dai, H. Gao, A simple electrochemical sensor based on rGO/MoS 2/CS modified GCE for highly sensitive detection of Pb (ii) in tobacco leaves, RSC Adv. 11 (2021) 29590–29597.